

Radiation Source Localization in GPS-denied Environments using Aerial Robots

Frank Mascarich¹, Taylor Wilson², Christos Papachristos³, and Kostas Alexis⁴

Abstract—This paper details the system and methods developed to enable autonomous nuclear radiation source localization and mapping using aerial robots in GPS-denied environments. A Thallium-doped Cesium Iodide (CsI(Tl)) scintillator and a Silicon Photomultiplier are combined with custom-built electronics for counting and spectroscopy, and the provided radiation measurements are pose-annotated using visual-inertial localization enabling autonomous operation in GPS-denied environments. Provided this capability, a strategy for radioactive source localization, as well as active source search path planning was developed. The proposed method is motivated and accounts for the limited endurance of the vehicle, which entails a very small amount of dwell points, and the fact that GPS-denied localization implies varying uncertainty of the robot's position estimate. The complete system is evaluated in multiple experimental studies using a small aerial robot and a Cesium-137 radiation source. As shown, accurate radioactive source localization is achieved, enabling efficient radiation mapping of indoor GPS-denied environments.

I. INTRODUCTION

Nuclear sites, active, decommissioned, or scheduled for decommissioning, represent major assets and critical facilities requiring rigorous, systematic and comprehensive inspection that necessitate radiometric surveying. Examples include the nuclear enrichment and waste storage facilities of the Manhattan Project, active nuclear power stations, and the sites of nuclear disaster. Robotized nuclear site inspection ensures the safety of personnel, advances the systematicity of the inspection process, enables repeatable monitoring missions, facilitates access in highly radioactive environments, and allows rapid and comprehensive search at low cost.

In the literature multiple efforts can be identified, largely based on automatically guided or teleoperated ground robots [1–3], unmanned aerial vehicles operating in open-ended GPS-supported environments [1, 4], underwater robots for pipe inspection [5] and more. Despite the significant progress and pioneering efforts of the community, reliable robotic autonomy and information gathering in the complex, cluttered, often highly contaminated and GPS-denied nuclear sites remains particularly challenging. Iconic examples are the “sarcophagus” of Chernobyl's Unit 4, the recent efforts to inspect the Fukushima Daiichi nuclear power plant, and the need to inspect the nuclear waste storage facilities at the Hanford Site.

This material is based upon work supported by the Department of Energy under Award Number [DE-EM0004478].

^{1,3,4} The authors are with the Autonomous Robots Lab, University of Nevada, Reno, 1664 N. Virginia, 89557, Reno, NV, USA fmascarich@nevada.unr.edu

² The author is with the Wilson Laboratory for Radiation Physics, University of Nevada, Reno, 1664 N. Virginia, 89557, Reno, NV, USA

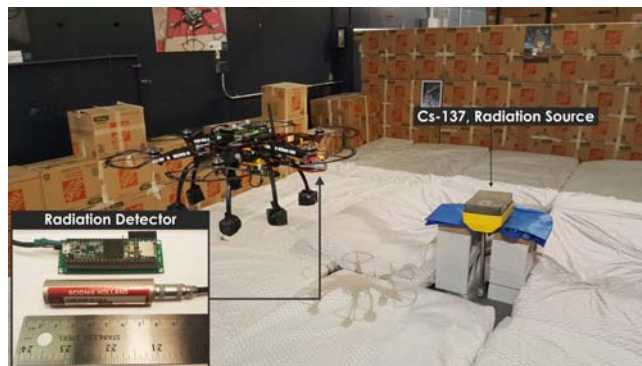


Fig. 1. Instance of experiment for autonomous active search and radioactive source localization using a small aerial robot integrating a miniaturized CsI(Tl) scintillator operating in a GPS-denied environment.

This work contributes the system design and algorithmic solutions to enable small aerial robots to conduct autonomous radiation detection, source localization, 3D/radiation mapping, and active source-seeking behavior in indoor, GPS-denied environments. A miniature Thallium-doped Cesium Iodide (CsI(Tl)) scintillator combined with a Silicon Photomultiplier (SiPM) allows radiation measurement and detection and is interfaced through an in-house designed counting and spectroscopy circuit. Its data are combined with the localization estimates of a visual-inertial localization and mapping unit to derive pose-annotated radiation measurements in GPS-denied areas.

Due to the limited endurance of small aerial robots and the need for long dwelling times to allow the radiation counting statistics to provide reliable estimates, a source localization method tailored to operate with a very limited number of measurements is developed. The proposed method further exploits the fact that the robot derives a volumetric occupancy map of its environment in real-time which enables to a) constrain the problem of source localization (considering solid sources), b) better handle the existence of objects with materials that attenuate the radiation levels (shielding), and also c) develop a volumetric map of the environment annotated with expected radiation intensity levels. Finally, precisely due to the necessarily small number of radiation measurements, an active source localization informative path planning strategy in environments for which no prior map is available is developed. The overall system and methods are evaluated in experimental studies using a small aerial robot and real radiation sources.

The remainder of this paper is structured as follows:

Section II provides an overview of related work, while the developed radiation detection and mapping sensor unit is presented in III. The proposed source localization and active source-seeking algorithms are detailed in Section IV, followed by experimental evaluation in Section V. Finally, conclusions are drawn in Section VI.

II. RELATED WORK

The topic of radiological source localization has been studied through a set of contributions including those in [6–10]. Among them, maximum likelihood estimation is utilized in [7, 8, 10], numerical adjoints in conjunction to a bayesian formulation are used in [6], while a particle filter is employed in [7]. In all of these strategies, a large number of sensor measurements per iteration of the localization method is required. Typically these radiation measurements are considered to be provided by a fixed array of sensors. Aiming to address the questions of sensor deployment and multi-robot guidance, the works in [11, 12] present a framework for relevant information-gathering tasks. Active source (e.g. radiological, chemical) localization has been studied in [13–15]. Sequential testing theory is utilized in [16, 17]. In the specific field of nuclearized robotics, a set of works [1, 2, 4, 18–21] have presented interesting results. The authors in [18] describe a distributed guidance strategy by means of information gradients to estimate the distribution of radiation and tested their method using light as a “radiation analog” source. The works in [19, 21] aim to handle multiple sources and evaluate their method in simulation. The authors in [1] employ semantic scene segmentation based on aerial robotic data in order to better inform the information gathering trajectories of a ground robot (and broadly an aerial-ground robot team). The work in [20] uses an RMAX helicopter to map radiation over large environments. The contribution in [4] refers to post-disaster radiation mapping also using an RMAX helicopter combined with a grid-based Bayesian estimator for single source localization and contour analysis for multiple source handling, while the presented results refer to 2D radiation mapping and source localization. Finally, research activities such as those in [2] aim to address the problem of 3D mapping and remote access in highly contaminated sites.

The solutions detailed above require large aerial vehicles which map macro-sized geographic areas with a low resolution understanding of the contamination, or an expansive network of sensors which utilize a large number of measurements to estimate the covered area’s radiation field. The contribution of this paper refers to a) the integration of radiation detection and source localization with the GPS-denied navigation capabilities onboard a small aerial robot, b) an online 3D source localization and mapping method that is tailored to the limited amount of measurements that can be provided by small aerial robots and further exploits the availability of the real-time reconstructed volumetric map, as well as c) informative path planning for source seeking behavior in cluttered and geometrically complex spaces.

III. ONBOARD RADIATION DETECTION

The developed system that enables onboard radiation detection and source localization is presented in this section.

A. System Overview

The system developed consists of a small hexarotor platform with a take-off weight of 2.6kg. The robot is equipped with the developed radiation detection system further detailed below. A Pixhawk-autopilot is employed for the attitude control, while an Intel NUC5i7RYH and a stereo visual-inertial sensor are integrated. The visual-inertial sensor provides synchronized stereo frames (using a StereoLabs ZED) that are then software synchronized with the IMU data (UM7). All the planning, localization and mapping, and position control loops are running on the NUC5i7RYH and with the support of the Robot Operating System (ROS). The system performs visual-inertial odometry using ROVIO [22] and mapping through the point cloud from the stereo camera and the robot pose estimates. The environment is represented using an occupancy map \mathcal{M} [23] with voxels m of edge length r . For position control, the linear model predictive controller described in [24] is utilized.

The choice of radiation detector for this research was driven by three main considerations, namely a) sensitivity, b) weight and power consumption, as well as c) spectroscopic resolution. Scintillation detectors for gamma radiation offer high sensitivity. Selecting and integrating a new generation scintillator and photosensor, we demonstrate a highly efficient detector package for miniaturized robots that weighs 41g including the counting and spectroscopy electronics.

For this work, a Thallium-doped Cesium Iodide (CsI(Tl)) scintillator was used and it offers spectroscopy-grade energy resolution and timing. The complete detector system consists of a) a Scionix V10B10 CsI(Tl) scintillation crystal, a small SiPm, and a preamplifier integrated in a 18g, cylindrical package (66mm long, 16mm wide), as well as b) a custom-designed pulse counting and spectroscopy circuit which weighs 23g. The scintillator has a voltage output in which pulses correspond to gamma photons interacting with the scintillation crystal. These pulses have amplitudes proportional to the energy of the gamma photon unique to each radionuclide. Therefore for spectroscopy, not only must the counting circuit count the number of pulses present on the scintillators output, it must also log the amplitude of the pulses. The pulse counting circuit is a series of 32 comparators which compare reference voltages generated by a resistor ladder against the output signal from the scintillator pre-amplifier. The outputs of the comparators are read by a 32-bit, 180 MHz ARM microcontroller and the system can discern between 32 different pulse amplitudes, therefore enabling spectroscopy and separate counting of gamma radiation at different energy levels. Updated measurements are reported by the microcontroller at 10Hz.

B. Radiation Counts

A radiation detector is used to detect, track, and identify high-energy particles from radioactive materials. In the

case of this work, gamma-detection is considered and the observed radiation counts received by the detector can be modeled as a mixture of the signal from the radioactive source and the natural background radiation [25, 26].

The radiation counts received due to a radioactive source s by a symmetric detector at a position \mathbf{p}_k follows a homogenous Poisson process [25, 27] with mean intensity rate per time unit being equal to:

$$E(y_s^{\mathbf{p}_k}) = \frac{Aev_s}{4\pi\|\mathbf{p}_k - \mathbf{p}_s\|^2} \quad (1)$$

where A and e are the area and the efficiency of the detector, v_s is the source intensity, and $\|\mathbf{p}_k - \mathbf{p}_s\|^2$ denotes the euclidean distance from the detector to the source. Considering that the dwell time of detection period is T_D^k , then the expected total number of counts $E(Y_s^{\mathbf{p}_k})$ at the detector due to the source will be:

$$E(Y_s^{\mathbf{p}_k}) = T_D^k \frac{Aev_s}{4\pi\|\mathbf{p}_k - \mathbf{p}_s\|^2} \quad (2)$$

while the detector also receives radiation from the natural background (also a Poisson distribution) that takes the form:

$$E(Y_b^{\mathbf{p}_k}) = T_D^k Aev_b \quad (3)$$

where v_b is the background intensity. Since signals due to the source and background are independent, the total radiation counts remains a Poisson distribution and the expected value for the T_D^k period takes the form:

$$E(Y^{\mathbf{p}_k}) = E(Y_s^{\mathbf{p}_k} + Y_b^{\mathbf{p}_k}) = T_D^k Ae \left(\frac{v_s}{4\pi\|\mathbf{p}_k - \mathbf{p}_s\|^2} + v_b \right) \quad (4)$$

The quantities A and e of Eq (4) are determined by the calibration of the detector in a pre-characterized chamber. The intensity v_s is completely determined by the radioactive source and is therefore unknown. The background intensity rate v_b can be derived through preliminary measurements away from the expected radiation source (exploiting the fast decay of the inverse square law). Due to the fact that the measurement process is governed by a Poisson distribution, the role of dwell time is critical to ensure reliable measurements through averaging of the counting statistics. For every dwell position \mathbf{p}_k , the reading $y_s^{\mathbf{p}_k}$ is averaged over T_D^k , background is subtracted and the average value λ_k is used for source localization purposes.

C. Detector Calibration

The Scionix V10B10 has a voltage output consisting of pulses with a width of $2.2\mu s$ and an amplitude proportional to the energy of the gamma photon that triggered the pulse. This is the basic principle of gamma spectroscopy - different radioactive sources produce different amplitude spectra dependent on their energy. The frequency of the pulses, reported in Counts Per Second (CPS), is proportional to the level of gamma photons, or the intensity of the field.

Therefore, calibration of such a scintillator occurs in two steps, a dosimetric calibration, and an energy calibration.

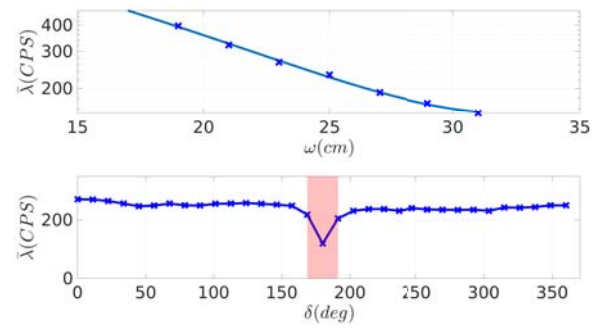


Fig. 2. Upper plot: Results of the first step of the count calibration in which the scintillator's dose rate response ($\bar{\lambda}$), measured in counts per second (CPS), at distances 19cm to 31cm from the source was evaluated. The scintillator is placed in a calibration chamber with the head of the scintillator directly facing the source. The data gathered, presented in a lin-log plot, shows that the count rate complies with inverse square law. Lower plot: Results of the second step of count calibration in which the scintillator's dose rate response ($\bar{\lambda}$) over various orientations (δ) was evaluated. Data is collected at various orientations to the source and reveals a symmetric response for all angles apart from a narrow cone of reduced sensitivity when the scintillator faces directly away from the source.

The purpose of dosimetric calibration is to determine the scintillator's efficiency. For accurate source localization and more importantly field intensity estimation, it is necessary to determine the relationship between a scintillator's count rate, and the true dose rate of the field. To determine this relationship, the scintillator is placed in a calibration chamber which contains a radioactive source and pre-characterized dose rate characteristics at various positions.

There are two sub-steps in a dosimetric calibration. The first is to determine the count rate with the scintillator at an ideal orientation directly facing the source. The scintillator is placed at various distances from the source, and count rates are recorded over long dwell times. The second step relates to determining the directionality of the scintillator in response to its shape and the position of the integrated electronics. The scintillator is placed at a single distance from the source and is rotated around its yaw axis. Variation around its roll angle is not required due to the symmetrical nature of the scintillation crystal.

The results of this calibration procedure on our scintillator are shown in Figure 2. As shown, the scintillator has a dose rate response in agreement with the inverse square law of radiation propagation, and from this calibration we can extract the expression which transforms counts from the scintillator into the true dose rate of the field. The results also reveal a mostly symmetric orientation response with roughly 50% decrease in detected counts over a small arc of orientations when its back faces the source (due to the interfacing electronics inducing a shielding effect). The latter results in a cone of reduced sensitivity to sources located directly behind the sensor.

The second step of a scintillator calibration determines the energy response of the scintillator when exposed to different radioactive sources. While sources of a particular energy will produce pulses of varying amplitude due to back-scattering

and other effects, there will be a dominant amplitude in a subset of the channels. This dominant subset will be characteristic for a particular energy level. Figure 2 shows results of this calibration for Cobalt-60, and Cesium-137.

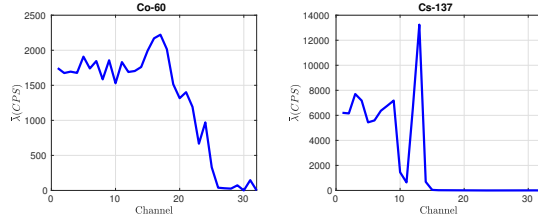


Fig. 3. Plot showing the results of the energy calibration in which the scintillator's energy response to different gamma sources was evaluated. Specifically, the cases for Cobalt-60 and Cesium-137 are shown and the different peak energy channels are presented.

D. Sources of Error and Noise

For a certain detector, a number of reasons for fluctuation in the response exist. Those include a) possible drift of the operating characteristics, b) sources of random noise within the interfacing electronics, c) dead times due to the time required to separate two interaction events, and d) statistical noise arising from the discrete nature of the measured signal (which follows a Poisson distribution) [25]. The latter typically is the most significant and represents an irreducible minimum amount of fluctuation that will necessarily be present in the detector signal despite the quality of the scintillator and interfacing circuitry. This arises from the fact that the charge generated within the detector by a quantum of radiation is not a continuous variable but rather represents a discrete number of charge carriers. A Poisson distribution models the effect and for a mean value λ_k , the variance is λ_k and the standard deviation is $\sqrt{\lambda_k}$. For multiple measurements acquired at a certain point, the Poisson distribution can be approximated by a Gaussian one.

E. Automated Dwell Time Calculation

As the variance of the measurement follows its mean, more measurements must be acquired at higher count rates to ensure a reliable estimate. Therefore, for robot locations at higher radiation levels, longer dwell times are required. To automatically adjust the dwell time T_D^k , the system calculates the derivative of the mean of the signal $y^{\mathbf{p}^k}$ and considers T_D^k to be sufficient once $\dot{y}^{\mathbf{p}^k} < y_{\text{thres}}^{\mathbf{p}^k}$ over a duration $t_D^{\text{thres}} > t_D^{\text{min}}$. This allows the robot to optimally use its limited endurance, dwelling for a short period of time at areas of decreased radiation intensity (and therefore small variance) and longer times in the presence of stronger fields.

IV. SOURCE LOCALIZATION AND ACTIVE SOURCE SEARCH

Provided the ability of the robot to acquire radiation detection measurements, counting and spectroscopic, alongside its capability to operate in a GPS-denied manner and map its environment, a strategy for radioactive source localization as well as active source search was developed. The proposed

strategy is motivated and accounts for the limited endurance of the vehicle which entails a very small amount of dwell points and the fact that GPS-denied localization implies varying uncertainty of the robot's own position estimate.

A. Radiation Source Localization

A source localization method designed around key limitations of aerial robots operating in GPS-denied environments is proposed. It is specifically motivated from the fact that a) limited flight endurance implies a constrained set of dwell points \mathcal{P}_d^k especially because long dwell times are required for reliable measurements, as well as b) the localization uncertainty of the robot, alongside c) the inherent variance of radiation detection which increases with the intensity of the measurement as described by the Poisson distribution statistics. Given that for increased intensity values, longer dwell times are needed, which further challenges the endurance of the robot, the ability of the method to operate with a very limited set of measurements is crucial.

The source localization algorithm begins when the robot first acquires three radiation readings that are above background at different dwell point locations. The averaged radiation reading λ_k (background effect removed) is used. A main challenge of source localization methods is to appropriately use multiple measurements to disambiguate between possible source locations. Given a single intensity reading, distinguishing between the cases of a weak source close to the robot, or a stronger source far away is not possible. The key insight of the method is that provided at least three measurements at different locations with variation among all axes, there will be a single point that satisfies the inverse square law for all three measurements in an environment with a single radioactive source and no shielding materials. Expressed geometrically, there will be a single point of intersection between three spheres corresponding to the same intensity but each of them centering at a different measurement point. Below, the algorithmic steps leading to source localization are detailed and summarized in Algorithm 1.

In this framework, the first step of the proposed approach is to spawn sets $\{\mathcal{S}^k\}$ of N concentric spheres for each of the dwell points $\mathbf{p}_k \in \mathcal{P}_d^k$. Each sphere in each of these sets corresponds to a certain intensity and radius from its associated dwell point. Subsequently, the algorithm identifies the set of all possible points \mathcal{I} that lie on the circles defining the intersections between spheres which center on different dwell locations but have matching intensities. Discretization of the spheres' radii and the circles of intersections is used for efficient calculation.

Given the locations of the intersection points $\mathbf{p}_I^j \in \mathcal{I}$ and considering each of them as a possible source location, the method then estimates the expected radiation reading at all dwell points from each point of intersection. For all dwell points, using the normal distribution of radiation readings centered around the dwell point's average value $\bar{\lambda}_k$ and associated standard deviation σ_{λ_k} , the value $\rho^{\mathbf{p} \rightarrow \mathbf{p}^k}$ of the probability density function (PDF) of the expected reading $\lambda_{\mathbf{p}_I^j \rightarrow \mathbf{p}^k}$ is calculated against all intersections (each of which

Algorithm 1 Source Localization Algorithm - Iteration

```
1: for all  $\mathbf{p}_k \in \mathcal{P}_d^k$  do
2:   spawn spheres  $\mathcal{S}(\mathbf{p}_k)$ 
3: end for
4: for all combinations of  $\mathbf{p}_k$  do
5:   find the set  $\mathcal{I}$  of intersection points  $\mathbf{p}_j$ 
6: end for
7: for all combinations of  $\mathbf{p}_j \in \mathcal{I}$  and  $\mathbf{p}_k \in \mathcal{P}_d^k$  do
8:   calculate expected reading  $\tilde{\lambda}_{\mathbf{p}_j \rightarrow \mathbf{p}_k}$ 
9:   derive normal distribution  $\mathcal{N}(\tilde{\lambda}_k, \sigma_{\lambda_k})$ 
10:  derive  $\rho^{\mathbf{p}_j \rightarrow \mathbf{p}_k} \leftarrow \text{PDF}(\mathcal{N}(\tilde{\lambda}_k, \sigma_{\lambda_k}), \tilde{\lambda}_{\mathbf{p}_j \rightarrow \mathbf{p}_k})$ 
11: end for
12: for all  $\mathbf{p}_j \in \mathcal{I}$  do
13:   derive average probability  $\bar{\rho}_j$ 
14: end for
15:  $\mathcal{I}' \leftarrow \{\mathbf{p}_j \in \mathcal{I} : \bar{\rho}_j \geq \alpha \max(\{\bar{\rho}_j\})\}$ 
16: derive centroid  $c$  of  $\mathbf{p}_j \in \mathcal{I}'$  and associated  $\sigma_c$ 
17: derive  $\mathcal{I}^{opt}$  by removing outliers from  $\mathcal{I}'$ 
18: derive centroid  $\mathbf{p}_s$  of  $\mathbf{p}_j \in \mathcal{I}^{opt}$ ,  $\sigma_s$  and intensity  $\bar{\lambda}_s$ 
19: test new source estimate  $[\mathbf{p}_s, \sigma_s, \bar{\lambda}_s]$ 
20: (identify centroid  $\mathbf{p}_m^s$  of closest voxel  $m$  in map  $\mathcal{M}$ )
21: ( $\mathbf{p}_s \leftarrow \mathbf{p}_m^s$ )
22: Return  $[\mathbf{p}_s, \sigma_s, \bar{\lambda}_s]$ 
```

are considered as a possible source location). A cumulative set Λ_I^j of such probabilities $\{\rho^{\mathbf{p} \rightarrow \mathbf{p}_k}\}$ for all intersection points is derived and the average value $\bar{\rho}_j$ is calculated. Then, the set of averaged probabilities Λ_I is formulated.

Provided this set, the method sorts the probabilities $\bar{\rho}_j$ and chooses the top subset given a tunable factor α defining the proportion of values in this subset. Then the probabilistically-weighted centroid of locations of these intersection points is derived along with its standard deviation. Searching within the selected subset of the intersecting points, the algorithm checks if its location lies within the bounds of one standard deviation and only then it considers it as part of a new set \mathcal{B} of possible final estimation results for the source location and intensity (otherwise considered as an outlier). Subsequently, the centroid \mathbf{p}_s of locations of the points in \mathcal{B} is found alongside the average intensity $\bar{\lambda}_s$. This tuple $[\mathbf{p}_s, \sigma_s, \bar{\lambda}_s]$ corresponds to the new estimate regarding the source location and its expected intensity.

Before it is returned as the new best estimate, the tuple $[\mathbf{p}_s, \sigma_s, \bar{\lambda}_s]$ is tested in terms of reducing the following error metric:

$$\epsilon = \frac{1}{k} \sum_{i=1}^k \|\lambda_k - \hat{\lambda}_{\mathbf{p}_s \rightarrow \mathbf{p}_k}\|^2 \quad (5)$$

where $\hat{\lambda}_{\mathbf{p}_s \rightarrow \mathbf{p}_k}$ denotes the expected radiation reading at \mathbf{p}_k given the source estimate $[\mathbf{p}_s, \sigma_s, \bar{\lambda}_s]$. As long as this error metric is improved between subsequent iterations, the new source estimate becomes the output of the method. Furthermore, if significant increase in this metric is detected and by performing ray casting on the map (when available for

the relevant subset of the environment) it is found that there is an object occluding the latest dwell point with the previous source location, that dwell point is considered uninformative or influenced by external factors (e.g. radiation shielding materials) and is therefore dropped.

Finally, if the area around the source estimate \mathbf{p}_s has been explored, the robot finds the closest occupied voxel m in the occupancy map \mathcal{M} . Its centroid \mathbf{p}_m^s updates the source location estimate, a procedure that exploits the fact that sufficiently accurate maps are derived online and only solid radiation sources are considered. The whole procedure is then iteratively repeated at the next dwell point.

B. Radioactive Source Search

For the robot to be able to efficiently detect and estimate the radioactive source location and intensity, informative measurements are required. In this work, we evaluated both fixed-lattice patterns when the environment is considered to be known, and propose a new active radioactive source search path planner for the cases of initially unknown environments. This section focuses on the latter part, while the experimental results also present studies with fixed-lattice trajectories.

1) *Environment Representation and Mapping*: The environment is volumetrically represented in an occupancy map \mathcal{M} that consists of cubical voxels $m \in \mathcal{M}$ with edge length r . Each voxel is considered as either “unexplored”, “free” or “occupied”. Update of the map relies on the onboard localization of the system that exploits visual-inertial cues and depth data coming from a stereo camera. The robust odometry framework in [22] is employed to estimate the robot pose \mathbf{p}_k . This volumetric map representation is used for autonomous robot planning.

2) *Initial Area Exploration*: When the robot is requested to identify and estimate the source location and intensity in unknown environments, a set of initial steps take place that allow it to explore the space until radiation measurements above background are detected. For this particular step, we employ our previous work related to next-best-view path planning [28] with the only difference being that the robot dwells at each planned exploration viewpoint for time T_D^k adaptively calculated according to Section III-E. This step is disengaged once three radiation readings λ_k at respective dwell points above background are detected and enable a first estimate of the source location. At this point, the source localization algorithm has returned its first estimate $[\mathbf{p}_s, \sigma_s, \bar{\lambda}_s]$ regarding the radioactive source location and strength.

3) *Active Source Search*: Provided the current source estimate $[\mathbf{p}_s, \sigma_s, \bar{\lambda}_s]$ and occupancy map \mathcal{M} , a path planning approach is proposed and aims to derive informative next dwell points and collision free paths for the robot to efficiently inform the subsequent iteration of the source localization method. The proposed planner accounts for certain facts and limitations, namely: a) the fact that only a limited set of measurements can possibly be acquired due to the endurance constraints of the robot, b) the importance of sufficient dwell time to ensure that reliable radiation readings are derived

without compromising the battery life of the robot, as well as c) the localization uncertainty of the robot as represented by the covariance matrix of its position Σ_p . Furthermore, it aims to ensure progress in the exploration mission which then ensures that new collision free trajectories can be identified and the map within which the source lies is -to a large extent- explored. Planning takes place in the configuration space of positions and heading of the robot, that is $\xi = [x, y, z, \psi]$ assuming small roll and pitch angles.

Given the latest map \mathcal{M} , the planner starts from the current robot configuration ξ_0 and incrementally builds a geometric random tree \mathbb{T} with maximum edge length ℓ . The resulting tree consists of N_T nodes n_i , associated robot configurations ξ_i and a set of collision free paths μ . A minimum of N_{\min} and maximum of N_{\max} nodes are defined to ensure sufficient exploration of the configuration space and low computational times. During the tree spanning process, yaw rate constraints $\dot{\psi}_{\max}$ are respected given a constant linear velocity v_t . The proposed information gain of a node n_i is denoted as $\mathbf{Gain}(n_i)$ and takes the form:

$$\mathbf{Gain}(n_i) = \frac{r_{i \rightarrow s}^2}{\delta^2} e^{-\frac{r_{i \rightarrow s}^2}{\delta^2}} \prod_{j=0, j \neq i}^{N_d^k} e^{-\frac{r_{i \rightarrow j}^2}{2N_d^k}} \quad (6)$$

where $r_{i \rightarrow j} = \|\xi_i - \xi_j\|^2$ the distance between the sampled configurations x_i, x_j at nodes n_i, n_j , $r_{i \rightarrow s} = \|\xi_i - \xi_s\|$ the distance of the sampled configuration ξ_i to the source, ξ_s is the configuration corresponding to the estimated source location \mathbf{p}_s , N_d^k is the current number of dwell points, and δ, ζ are tunable factors that control the maximum of the function. The node n_{opt} that maximizes this gain is selected and the associated collision free path μ_0^{opt} leading to ξ_{opt} is extracted. This path is sampled at ν points and a set of q yaw angle orientations are randomly sampled at each new vertex. Subject to the maximum yaw rate $\dot{\psi}_{\max}$, the method then identifies the sequence of yaw angle orientations that simultaneously maximize the unexplored volume to be covered based on the exploration gain described in our previous work in [28]. The robot is then commanded to follow this path, dwell at ξ_{opt} and perform a new step of source localization, while the whole process is repeated iteratively. Through the proposed gain, dwell points that a) approach the expected source location while avoiding points very near the source estimate as the robot has localization uncertainty and very high radiation readings require longer dwell times, and b) keep distance from all the previous dwell points are identified. Figure 4 depicts an illustrative example.

In addition, to ensure further robustness against increased localization uncertainty of the robot and its correlation with a possibly wrong estimate of the distance from the source, which has significant influence due to the inverse square law of radiation propagation, nodes sampled closer than 1 semi-major axis of the ellipsoid corresponding to the position covariance Σ_p are considered invalid. Similarly, any nodes corresponding to a robot configuration that would lead to a measurement $\lambda_k < \lambda_{\min}$, $\lambda_{\min} \rightarrow 0$ given the current

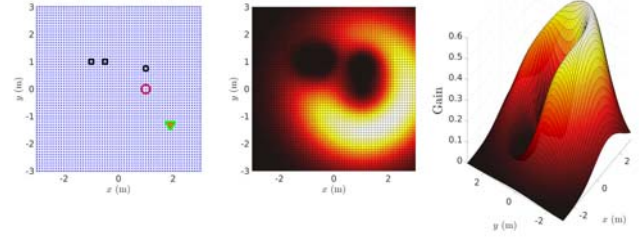


Fig. 4. Illustrative example of the next-best-dwell-point location selection using the proposed gain formulation. In this example, a 3×3 m grid with equally-spaced dwell candidates (blue 'x' marker) are evaluated given the current source location (red 'o' marker) and three previous dwell points (black 'x' marker) is considered, while $\delta = 1$ and $\zeta = 1.85$. The next-best-dwell-point is indicated (green 'v' marker), while a surface plot of the gain over all possible locations is simultaneously presented. As shown, the method accounts for the previous locations of the dwell points and the estimate of the source therefore selecting a next dwell location that provides information from a significantly different part of the map and a varied distance from the source.

source estimate are also eliminated. Overall, this imposes a geometric constraint ensuring that the next dwell point will not a) be too far from the expected source location risking the possibility of getting a measurement close to background, and b) will not be very close to the source making its inherent localization uncertainty a reason for erroneous estimation.

V. EXPERIMENTAL EVALUATION

Three experiments were conducted to evaluate the performance of the system, the source localization algorithm, as well as the active source search path planner. Each experiment was performed in an indoor environment using a Cs-137 source measuring roughly $618.1 \mu\text{R/h}$ at a distance of 0.65m . The source is a non-destructive testing device commonly used in civil engineering and projects a hemispherical radiation field facing upward when the source is exposed.

The first experiment consists of the robot flying in a predetermined fixed-lattice pattern in which the environment is assumed to be known. The fixed-lattice pattern is a series of nine measurement locations (dwell points), the first of which is a point just above background and the remaining eight points are in a grid surrounding the true source location. The second experiment consists of a similar fixed-lattice pattern with ten measurements, but also includes a L-shaped wall of cinder blocks partially surrounding the radiation source which serves to attenuate the radiation field by about 50% at measurement points on the opposite side of the wall from the source. Finally, the third experiment demonstrates the active source search path planner, and consists of five measurement points whose positions were determined autonomously online. It is noted that due to the requirement to dwell for several seconds (from 5s to 15s in these results), the robot is limited to derive the needed source estimate with typically less than 12 dwell points. The proposed localization and active search strategy was demonstrated to derive an accurate source estimate within the first four autonomously selected dwell points.

In each of the visualizations below, the robot's perception of the environment is expressed as an octomap [23]. Figure 5 visualizes the results of the first experiment in which the source was localized after the third measurement, at which point the error e_d in distance between the source estimate and the true source location was $e_d = 1.52\text{m}$. After the final measurement, this error in distance was reduced to $e_d = 0.32\text{m}$.

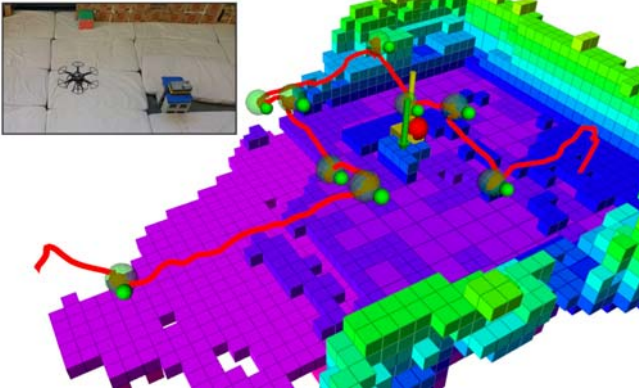


Fig. 5. Fixed-lattice source localization experiment without attenuating cinder blocks surrounding the source. The robot's trajectory is presented as a red line gathered from the robot's odometry data. Dwell points are represented as light green semi-transparent spheres with an adjoining solid green sphere representing the position of the sensor. The true source location is represented by a green arrow and is unknown to the source localization algorithm. Finally, the source location estimate is drawn as a solid red sphere, while the nearest voxel, and true source estimate is denoted by the yellow arrow positioned above a yellow cube.

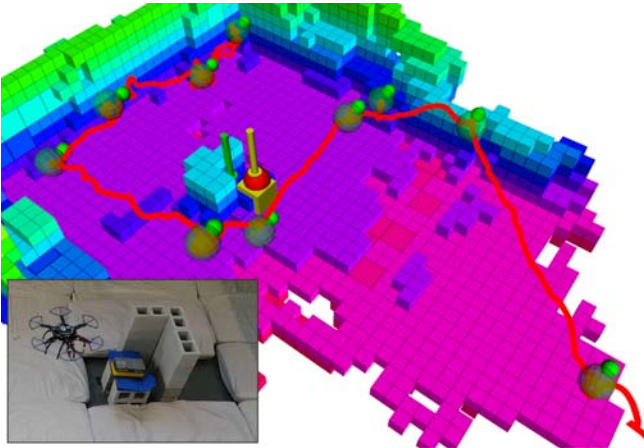


Fig. 6. Fixed-lattice source localization experiment with attenuating cinder blocks partially surrounding the source. Measurement points #6, #7, and #8 (where measurement point #1 is the point on the lower right side of the image) are shielded from the radiation source by the cinder block wall, and their readings are 50% lower than those expected given their position and the source's intensity. In this experiment, the final source localization error is 0.28m .

Figure 6 demonstrates that the localization algorithm performs sufficiently in the presence of partially attenuated readings given that a first set of non-attenuated measurements were acquired. Operation subject to partially attenuated measurements is achieved due to the additional step of the

localization method that checks and verifies if a new source estimate is in agreement with all the dwell points \mathbf{p}_k and associated radiation readings λ_k and drops a measurement if a significant disagreement is identified.

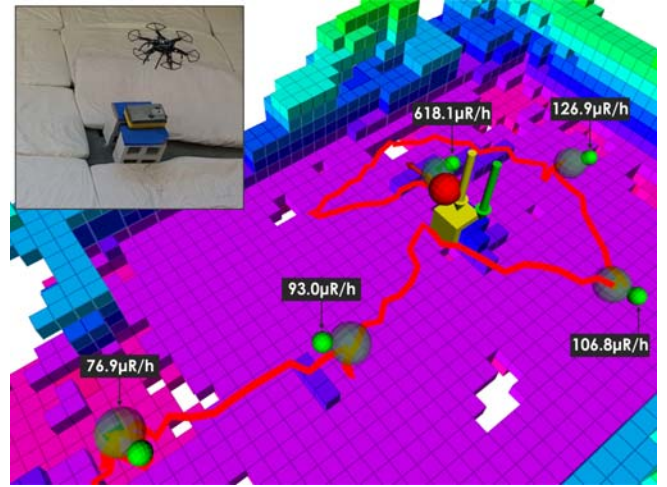


Fig. 7. Autonomous active source search experiment. The experiment is initiated through exploration paths using the exploration planner in [28]. Once three dwell points with radiation readings above background are identified, the method commands the robot to dwell, a first radioactive source estimate becomes available and subsequently the active source search for next-best-dwell-points is engaged. With only 5 dwell points, the method achieves an error of only $e_d = 0.31\text{m}$ in the position of the source.

Figure 7 shows the active source search algorithm in its entirety. At the final measurement, the localization error is 0.31m a result achieved with only 5 dwell points and associated radiation readings. Finally, Figure 8 presents a radiation map for the same experiment, using the source localization estimate (position and source strength) and the inverse square law to indicate the expected radiation level at different parts of the map. Overall, the aforementioned set of results illustrates the ability of the proposed system to conduct radioactive source localization in GPS-denied environments, as well as active source search in initially unknown and unmapped environments through a combination of first steps for exploration, subsequent identification of optimized dwell points and identification of intermediate yaw orientations that support the exploration process during the source seeking behavior. The complete set of recorded data are released as an open dataset to enable community re-utilization [29].

VI. CONCLUSIONS

This paper presented a system and method for localizing a radiation source in known and unknown environments using a small aerial robotic platform. The described method is able to localize a radiation source given a small number of measurements due to the limited flight endurance of the platform, and accounts for the robot's own position uncertainty in flight. Furthermore the algorithm achieves source localization in the presence of attenuated and inaccurate readings. The above described planner is able to identify optimal dwell points for measurement and greatly improves the abilities of

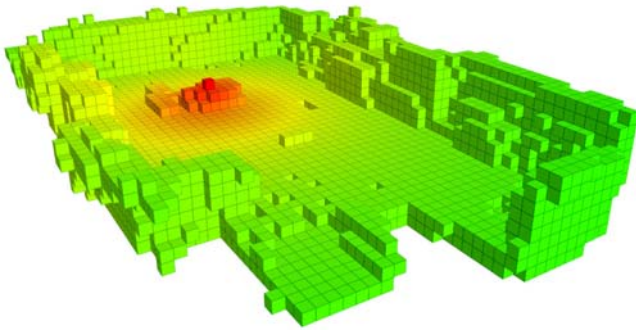


Fig. 8. Radiation mapping applied on the volumetric map based on the source localization estimate (location and source strength) and the inverse square law. This map is derived based on the source estimates and online maps derived during the autonomous active source search experiment and presents the potential of 3D/Radiation mapping using small aerial robots. It is noted that due to the fast decrease of radiation strength values as a result of the inverse square law, log-scale has been applied on the relevant values for better colormap representation.

the robot given the platform's endurance constraints. Finally, the robot exploits the real-time generated occupancy map to constrain the search space and achieve higher accuracy source localization.

Future work will include utilization of the spectroscopy abilities of the scintillator circuit to perform multi-source localization. Additionally, semantic classification can be utilized to further constrain the search space and improve the localization of the source using objects visible in the scene. Finally, methods to improve not only the position, but the intensity estimate of the source should be explored, especially in cases where measurements are partially attenuated.

REFERENCES

- [1] G. Christie, A. Shoemaker, K. Kochersberger, P. Tokekar, L. McLean, and A. Leonessa, "Radiation search operations using scene understanding with autonomous uav and ugv," *Journal of Field Robotics*, 2016.
- [2] M. Maimone, L. Matthies, J. Osborn, E. Rollins, J. Teza, and S. Thayer, "A photo-realistic 3-d mapping system for extreme nuclear environments: Chernobyl," in *Intelligent Robots and Systems, 1998. Proceedings., 1998 IEEE/RSJ International Conference on*, vol. 3. IEEE, 1998, pp. 1521–1527.
- [3] R. Guzman, R. Navarro, J. Ferre, and M. Moreno, "Rescuer: Development of a modular chemical, biological, radiological, and nuclear robot for intervention, sampling, and situation awareness," *Journal of Field Robotics*, vol. 33, no. 7, pp. 931–945, 2016.
- [4] J. Towler, B. Krawiec, and K. Kochersberger, "Radiation mapping in post-disaster environments using an autonomous helicopter," *Remote Sensing*, vol. 4, no. 7, pp. 1995–2015, 2012.
- [5] A. Mazumdar, M. Lozano, A. Fittery, and H. H. Asada, "A compact, maneuverable, underwater robot for direct inspection of nuclear power piping systems," in *Robotics and Automation (ICRA), 2012 IEEE International Conference on*. IEEE, 2012, pp. 2818–2823.
- [6] K. D. Jarman, E. A. Miller, R. S. Wittman, and C. J. Gesh, "Bayesian radiation source localization," *Nuclear technology*, vol. 175, no. 1, 2011.
- [7] H. Wan, T. Zhang, and Y. Zhu, "Detection and localization of hidden radioactive sources with spatial statistical method," *Annals of Operations Research*, vol. 192, no. 1, pp. 87–104, 2012.
- [8] H. E. Baidoo-Williams, R. Mudumbai, E. Bai, and S. Dasgupta, "Some theoretical limits on nuclear source localization and tracking," in *Information Theory and Applications Workshop (ITA)*. IEEE, 2015.
- [9] H. E. Baidoo-Williams, "Maximum likelihood localization of radiation sources with unknown source intensity," *arXiv preprint arXiv:1608.00427*, 2016.
- [10] G. Cordone, R. R. Brooks, S. Sen, N. S. Rao, C. Q. Wu, M. L. Berry, and K. M. Grieme, "Improved multi-resolution method for mle-based localization of radiation sources," in *Information Fusion (Fusion), 2017 20th International Conference on*. IEEE, 2017, pp. 1–8.
- [11] S. Martinez, J. Cortes, and F. Bullo, "Motion coordination with distributed information," *IEEE Control Systems*, 2007.
- [12] J. Cortes, S. Martinez, and F. Bullo, "Spatially-distributed coverage optimization and control with limited-range interactions," *ESAIM: Control, Optimisation and Calculus of Variations*, vol. 11, no. 4, pp. 691–719, 2005.
- [13] C. Zhang, D. Arnold, N. Ghods, A. Siranosian, and M. Krstic, "Source seeking with non-holonomic unicycle without position measurement and with tuning of forward velocity," *Systems & control letters*, 2007.
- [14] S. Pang and J. A. Farrell, "Chemical plume source localization," *IEEE Transactions on Systems, Man, and Cybernetics, Part B (Cybernetics)*, vol. 36, no. 5, pp. 1068–1080, 2006.
- [15] C. G. Mayhew, R. G. Sanfelice, and A. R. Teel, "Robust source-seeking hybrid controllers for autonomous vehicles," in *American Control Conference, 2007. ACC'07*. IEEE, 2007, pp. 1185–1190.
- [16] A. Kumar, H. G. Tanner, A. V. Klimenko, K. Borozdin, and W. C. Priedhorsky, "Automated sequential search for weak radiation sources," in *Control and Automation, 2006. MED'06. 14th Mediterranean Conference on*. IEEE, 2006, pp. 1–6.
- [17] R. Cortez, X. Papageorgiou, H. Tanner, A. Klimenko, K. Borozdin, and W. Priedhorsky, "Experimental implementation of robotic sequential nuclear search," in *Control & Automation, 2007. MED'07. Mediterranean Conference on*. IEEE, 2007, pp. 1–6.
- [18] R. A. Cortez, H. G. Tanner, and R. Lumia, "Distributed robotic radiation mapping," in *Experimental Robotics*. Springer, 2009.
- [19] A. A. R. Newaz, S. Jeong, H. Lee, H. Ryu, N. Y. Chong, and M. T. Mason, "Fast radiation mapping and multiple source localization using topographic contour map and incremental density estimation," in *Robotics and Automation (ICRA), 2016 IEEE International Conference on*. IEEE, 2016, pp. 1515–1521.
- [20] K. Vetter, D. Chivers, and B. Quiter, "Advanced concepts in multi-dimensional radiation detection and imaging," in *Nuclear Threats and Security Challenges*. Springer, 2015, pp. 179–192.
- [21] A. A. R. Newaz, S. Jeong, H. Lee, H. Ryu, and N. Y. Chong, "Uav-based multiple source localization and contour mapping of radiation fields," *Robotics and Autonomous Systems*, vol. 85, pp. 12–25, 2016.
- [22] M. Bloesch, S. Omari, M. Hutter, and R. Siegwart, "Robust visual inertial odometry using a direct ekf-based approach," in *Intelligent Robots and Systems (IROS), 2015 IEEE/RSJ International Conference on*. IEEE, 2015, pp. 298–304.
- [23] A. Hornung, K. M. Wurm, M. Bennewitz, C. Stachniss, and W. Burgard, "OctoMap: An efficient probabilistic 3D mapping framework based on octrees," *Autonomous Robots*, 2013.
- [24] M. Kamel, T. Stastny, K. Alexis, and R. Siegwart, "Model predictive control for trajectory tracking of unmanned aerial vehicles using ros," *Springer Book on Robot Operating System (ROS)*.
- [25] G. F. Knoll, *Radiation detection and measurement*. John Wiley & Sons, 2010.
- [26] G. J. Feldman and R. D. Cousins, "Unified approach to the classical statistical analysis of small signals," *Physical Review D*, 1998.
- [27] S. Fetter, T. B. Cochran, L. Grodzins, H. L. Lynch, and M. S. Zucker, "Gamma-ray measurements of a soviet cruise-missile warhead," *Science*, vol. 248, no. 4957, pp. 828–834, 1990.
- [28] A. Bircher, M. Kamel, K. Alexis, H. Oleynikova and R. Siegwart, "Receding horizon "next-best-view" planner for 3d exploration," in *IEEE International Conference on Robotics and Automation (ICRA)*, May 2016. [Online]. Available: <https://github.com/ethz-asl/nbvplanner>
- [29] F. Mascari, T. Wilson, C. Papachristos, and K. Alexis, "GPS-denied Radiation Source Localization Dataset." [Online]. Available: <https://github.com/unr-arl/radiation-source-localization-dataset>